INTERNATIONAL JOURNAL FOR NUMERICAL METHODS IN FLUIDS, VOL. 13, 1029–1053 (1991)

GREY-BODY SURFACE RADIATION COUPLED WITH CONDUCTION AND CONVECTION FOR GENERAL GEOMETRIES

MICHAEL ENGELMAN AND MOHAMMAD-ALI JAMNIA

Fluid Dynamics International, 500 Davis St. Suite 600, Evanston, IL 60201, U.S.A.

SUMMARY

This paper presents a numerical technique for the simulation of the effects of grey-diffuse surface radiation on the temperature field of fluid flows using FIDAP, a general purpose incompressible, viscous fluid code. The radiating surface relationships assume a non-participating medium, constant surface temperature and heat fluxes at the discretized elemental level.

The technique involves the decoupling of energy and radiation exchange equations. A concept of macrosurfaces, each containing a number of radiating boundary surfaces, is introduced. These boundary macroelements then carry the information from the radiating boundary into the fluid regime. A number of simulations illustrating the algorithm are presented.

KEY WORDS Grey-body radiation Finite element method Incompressible fluid flow Macrosurfaces

INTRODUCTION

Radiation heat transfer plays an important role in engineering. In some applications such as boilers, industrial furnaces, rocket propulsion, etc., the medium with its absorbing, emitting and scattering properties plays just as important a role as radiation exchange between the boundaries. In other types of problems such as honeycomb solar collector panels and automobile air-conditioning, only the radiation heat exchange between the boundary surfaces need be considered. Many authors[1–5] have considered participating media and have developed theories and solution methods for a variety of conditions. For a review paper on the recent advances in this area see Reference 6.

Reference 7 discusses radiation phenomena in great detail and presents the required theory, formulae and relationships for general and special cases. One of the special cases considered herein is when the radiating surfaces are grey-diffuse and the medium is non-participating. The work of Holland *et al.*[8] deals with honeycomb panels when radiation and conduction effects are coupled. This work is of both experimental and analytic nature.

Kassemi and Duval[9] studied the effects of wall radiation in crystal growth problems in a rectangular domain. References 10–13 considered the radiation heat transfer problem in Czochralski pullers. Crochet *et al.*[14] dealt with a similar problem in a vertical Bridgman furnace.

In this paper the finite element method is used to predict the non-participating medium's behaviour when the boundary surfaces are considered to be grey-diffuse and radiating. Of particular concern is the fact that the temperature field may be coupled with the flow field

0271–2091/91/181029–25$12.50

Received 13 September 1990
Revised 12 January 1991

through natural or forced convection. The concept of macrosurfaces is introduced; the macrosurface acts as an interface between the radiating boundary surface and the finite element boundary. Three problems are solved to test and verify the algorithm. A more realistic sample problem from the electronics industry is also solved which includes blocking surfaces as well as heat sources and buoyancy-driven flow. The results from this simulation are compared with the case when radiation is not taken into account.

GOVERNING EQUATIONS

Consider an enclosure consisting of N grey-diffuse surfaces with e_j as the emissivity of the jth surface. Suppose that the incompressible fluid enveloped by this enclosure is non-participating and that the view factor matrix is given by the F_{ij}-tensor. To evaluate the velocity, pressure and temperature fields in the fluid, the conservation equations of mass, momentum and energy in conjunction with appropriate boundary conditions are required:

momentum equation,

$$\rho\left(\frac{\partial u_i}{\partial t}+u_j u_{i,j}\right) = -p_{,i}+[\mu(u_{i,j}+u_{j,i})]_{,j}+\rho f_i-\rho g_i[\beta_T(T-T_0)], \tag{1a}$$

continuity equation,

$$u_{i,i}=0, \tag{1b}$$

energy equation,

$$\rho c_p\left(\frac{\partial T}{\partial t}+u_j T_{,j}\right) = (kT_{,j})_{,j}+q_s, \tag{1c}$$

boundary conditions,

$$u_i=\bar{u}_i, \qquad \sigma_i=\sigma_{ij}n_j=\bar{\sigma}_i, \qquad T=\bar{T}, \qquad q=-(kT_{,j})n_j=q_a+q_c+q_r, \tag{1d}$$

where c_p is the specific heat at constant volume, e_j is the emissivity of surface j, f_i is the body force vector, g_i is the gravitational force vector, k is the thermal conductivity, n_i is the surface normal vector, P is the fluid pressure, q_a is the applied heat flux, q_c is the convective heat flux, q_r is the radiative heat flux, q_s is the heat source, T is the temperature, T_0 is the reference temperature, t is time, u_i are Eulerian fluid velocity components, β_T is the thermal volume expansion coefficient, μ is the dynamic viscosity, ρ is the density, σ_{ij} is the stress tensor, σ_i is the surface stress vector and σ is the Stefan–Boltzmann constant.

For transient problems initial conditions are also required. In this paper we will restrict our attention to the energy equation and the associated radiation boundary conditions. For detailes on the momentum and continuity equations and their solution using the finite element method the reader is referred to Reference 15.

The energy equation relates the properties of the fluid to the temperature and how heat is being distributed in the fluid as well as from its boundaries. For a medium with grey-diffuse radiating boundaries, an additional equation is required which describes how the heat is being exchanged at the radiating boundaries regardless of the fluid. The heat exchange relationship between the radiating boundaries is given by

$$\sum_{j=1}^{N}\left(\frac{\delta_{ij}}{e_j}-F_{ij}\frac{1-e_j}{e_j}\right)q_j = \sum_{j=1}^{N}(\delta_{ij}-F_{ij})\sigma T_j^4, \quad i=1,\ldots,N, \tag{2}$$

where q_j is the radiative heat flux and T_j is the temperature of the jth surface. Note that the sum of the q_j computed in equation (2) is the q_r-term in the boundary condition equation (1d). Thus the coupling between the two equations is through the q_r-term. The derivation of equation (2) is discussed in detail by Siegel and Howell.[7] The major assumptions in deriving this equation are uniform temperature for each radiating surface as well as grey-diffuse surfaces.

It should be noted that equation (2) can only be solved once the view factors F_{ij} are known. The next section provides an outline of the techniques used to calculate the view factors.

VIEW FACTOR CALCULATIONS

Calculation of radiative energy exchange between any two surfaces requires determining the geometrical configuration factor, or view factor, between the two surfaces. For two black bodies the view factor is defined as the fraction of the diffusely distributed radiant energy leaving one surface i that arrives at a second surface j:

$$F_{ij}=\frac{1}{A_i}\int_{A_i}\int_{A_j}\frac{\cos\beta_i\cos\beta_j\,\mathrm{d}A_i\mathrm{d}A_j}{\pi r^2}, \tag{3}$$

where A_i and A_j are the areas of surfaces i and j respectively and β_i and β_j are the angles between the position-dependent normal vectors to surfaces i and j and a line of length r connecting the points of evaluation of the normals (see Figure 1).

The derivation of equation (3) can be found in Reference 7. The basic assumptions used in deriving equation (3) are (i) the two surfaces are diffusively emitting and reflecting and (ii) the two surfaces are isothermal. As a result of these assumptions, the view factor depends only on the

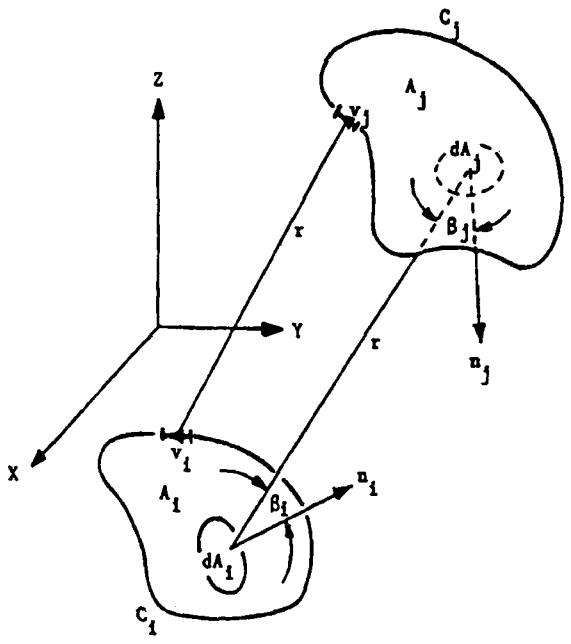

Figure 1. View factor calculation

geometry of the system. It is also important to note that for each surface i,

$$\sum_{j=1}^{N} F_{ij} = 1,$$

where N is the number of surfaces.

In the calculation of the view factors, equation (3) is not used directly; rather, different strategies are employed depending on whether the model is 3D, 2D or axisymmetric. Details of these algorithms and a complete discussion of the entire view factor calculation can be found in Reference 16. The view factor calculation in FIDAP is largely based on the FACET code.[16]

Shadowing algorithms

The major complication with the view factor calculation is the possibility of partial blocking or 'shadowing' between two surfaces by an intervening body. Three types of shadowing may exist between two surfaces: total self-shadowing, partial self-shadowing and third-surface shadowing. The various possibilities are illustrated in Figure 2. Total or partial self-shadowing can be detected between two surfaces by looking at the angles β_i and β_j (Figure 1). If $\cos \beta_i > 0$ and $\cos \beta_j > 0$, then the two surfaces can 'see' each other. This is equivalent to verifying that

$$r_{ij} \cdot n_i > 0 \quad \text{and} \quad r_{ji} \cdot n_j > 0, \tag{4}$$

where r_{ij} is defined in Figure 3. For N-sided plane polygons it is necessary to verify these dot product inequalities for all vectors r connecting the N corner points between the two surfaces, a total of $2N$ checks. If equation (4) is not satisfied for all r_{mn} $(m, n = 1, \ldots, N)$, then there is total self-shadowing. If equation (4) is satisfied for some r_{mn}, then there is partial self-shadowing.

For situations where partial self-shadowing or third-surface shadowing exists, the view factor can be calculated by first subdividing the two surfaces for which the view factor is being computed into n finite surfaces. Contributions to the view factor are not included for those surfaces in which

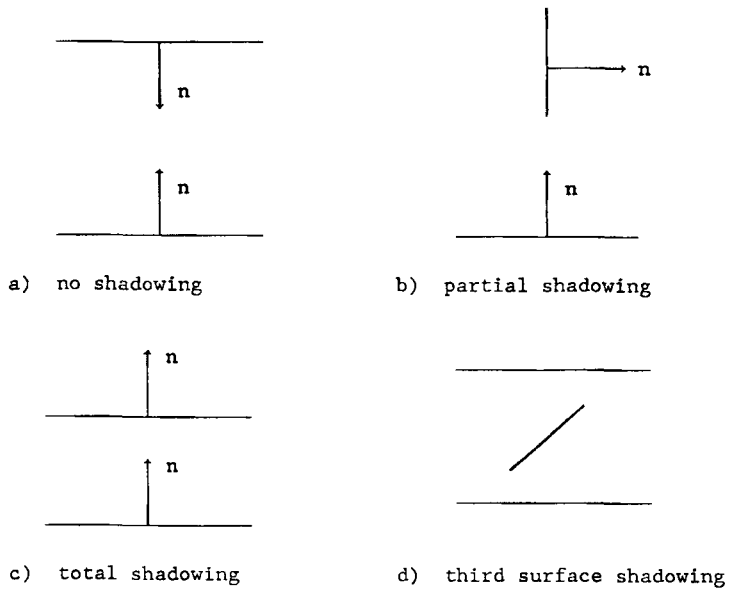

Figure 2. Surface orientations for shadowing

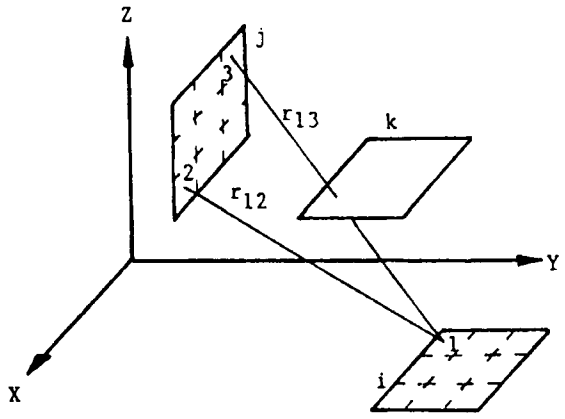

Figure 3. Third-surface shadowing

the ray r_{ij} fails to satisfy (4) or intersects with another surface—this procedure is illustrated in Figure 3. The computed view factor increases in accuracy as the number n of subsurfaces is increased.

Third-surface shadowing can be detected by determining if a line connecting the centroids of the two surfaces for which a view factor is being calculated intersects other enclosure surfaces. The accuracy of this detection scheme can be improved if the lines connecting the corner points of the polygon are also checked for intersection with other enclosure surfaces. Unless those surfaces that can be shadowing surfaces are specifically designated as blocking or obstructing surfaces, all enclosure surfaces must be checked for each pair of surfaces for which a view factor is being calculated. This can be a very time-consuming computation, particularly for three-dimensional geometries. Fortunately, the view factor computation is required only once for a given geometrical configuration.

FINITE ELEMENT IMPLEMENTATION

As noted earlier, the key equations required for the determination of the temperature field in the fluid are the energy equation and the radiation heat exchange equation. The energy equation is a continuum equation whereas the radiation heat exchange relationship is already a discrete equation. Therefore only the energy equation needs to be discretized using the finite element method. Applying the Galerkin finite element method in the usual fashion (refer to Reference 15 for complete details), the following set of matrix equations is arrived at:

$$\mathbf{M}\dot{\mathbf{T}} + \mathbf{K}\mathbf{T} + \mathbf{A}(\mathbf{u})\mathbf{T} = \mathbf{F} + \int_S q_r \boldsymbol{\vartheta}\, \mathrm{d}S, \tag{5}$$

where

$$\mathbf{M} = \int_V \rho c_p \boldsymbol{\vartheta}\boldsymbol{\vartheta}^{\mathrm{T}}\, \mathrm{d}V,$$

$$\mathbf{K} = \mathbf{K}_{11} + \mathbf{K}_{22}, \qquad \mathbf{K}_{ij} = \int_V k \frac{\partial \boldsymbol{\vartheta}}{\partial x_i} \frac{\partial \boldsymbol{\vartheta}^{\mathrm{T}}}{\partial x_j} \mathrm{d}V,$$

$$\mathbf{A}=\mathbf{A}_1(u_1)+\mathbf{A}_2(u_2), \qquad \mathbf{A}_i(u_j)=\int_V \rho c_p \vartheta u_j \frac{\partial \vartheta^T}{\partial x_i}\,dV,$$

$$\mathbf{F}=-\int_S (q_a+q_c)\vartheta\,dS+\int_V q_s \vartheta\,dV,$$

q_a is the applied heat flux, q_c is the convective heat flux, q_r is the radiative heat flux, q_s is the heat source term and ϑ is the element shape function vector for temperature.

The term $\int q_r \vartheta\,dS$ couples equation (5) with the radiative exchange equation (2). In the subsequent discussion the edge (or face) of an element on the edge of the computational domain will be referred to as a boundary element. Assuming that q_r is constant for a given boundary element, the energy and radiative exchange equations can be written

$$\mathbf{M}\dot{\mathbf{T}}+\mathbf{K}\mathbf{T}+\mathbf{A}(\mathbf{u})\mathbf{T}=\mathbf{F}-\mathbf{B}\mathbf{q}, \tag{6}$$

$$\mathbf{C}\mathbf{q}=-\mathbf{D}\mathbf{T}, \tag{7}$$

where

$$\mathbf{C}=(C_{ij}), \qquad C_{ij}=\frac{\delta_{ij}}{e_j}-F_{ij}\frac{1-e_j}{e_j},$$

$$\mathbf{D}=(D_{ij}), \qquad D_{ij}=(\delta_{ij}-F_{ij})\sigma T_j^3 \quad \text{(no summation on } j\text{)},$$

$$\mathbf{B}=(B_{kj}), \qquad B_{kj}=\int \psi \vartheta\,ds,$$

$$\mathbf{q}=(q_j).$$

In the above expressions the subscripts i and j pertain to the boundary elements (i.e. $i,j=1,N$) whereas the subscript k refers to the nodal points comprising the boundary radiating surfaces (i.e. $k=1,NB$, where NB is the total number of nodes defining the boundary elements). ψ is the shape function associated with the constant heat flux for each boundary element.

In matrix notation, for a steady state problem, equations (6) and (7) may be written as

$$\begin{bmatrix}\mathbf{A}_{11} & \mathbf{A}_{12}\\ \mathbf{A}_{21} & \mathbf{A}_{22}\end{bmatrix}\begin{bmatrix}\mathbf{T}\\ \mathbf{q}\end{bmatrix}=\begin{bmatrix}\mathbf{B}_1\\ \mathbf{0}\end{bmatrix}, \tag{8}$$

where

$$\mathbf{A}_{11}=\mathbf{K}+\mathbf{A}(\mathbf{u}), \quad \mathbf{A}_{12}=\mathbf{B}, \quad \mathbf{A}_{21}=(\delta_{ij}-F_{ij})\sigma T_j^3 \text{ (no summation on } j\text{)}, \quad \mathbf{A}_{22}=\mathbf{C},$$

$$\mathbf{B}_1=-\int_S (q_a+q_c)\vartheta\,dS+\int_V q_s\vartheta\,dV.$$

The main assumption in this formulation is that each element side (or face) at the boundary is a radiation surface which has constant properties.

In practice, the above approach has a number of serious drawbacks.

1. The radiation exchange equations couple the information of every node on the boundary to every other node on the boundary. If the matrix system (8) is solved as a coupled system, there will be a very substantial increase in the bandwidth of the global coefficient matrix, with an accompanying significant increase in computational cost.

2. The view factor calculations may become prohibitively expensive owing to the large number of radiating surfaces that have to be accommodated.
3. $\mathbf{D}(\mathbf{T})$ is highly non-linear.

To prevent the increase in bandwidth, rather than solving equation (8) as a fully coupled system, an alternative approach is to solve equation (7) first (for a given temperature field) and then use the resultant heat flux values in equation (6) as applied boundary conditions. This approach effectively decouples equations (6) and (7).

The decoupling of equation (8) as described above leads to the equations

$$\mathbf{A}_{11}\mathbf{T}=\mathbf{B}_1-\mathbf{A}_{12}\mathbf{q}, \tag{9}$$

$$\mathbf{C}\mathbf{q}=-\mathbf{D}\mathbf{T}. \tag{10}$$

These equations can now be solved in a sequential manner as follows.

(a) Equation (10) is solved for a 'given' temperature field.
(b) The calculated $\mathbf{q}$-vector is then used in equation (9) to calculate a new temperature field—the successive substitution (or Picard iteration) approach is used to solve equation (9). (It should be noted that equation (9) cannot be solved independently of the Navier–Stokes equations if convection exists.)
(c) Steps (a) and (b) are repeated until convergence is achieved.

Alternatively, a Newton–Raphson formulation for solving equations (9) and (10) can also be employed. In this case the equations to be solved become

$$\mathbf{J}\begin{bmatrix}\Delta\mathbf{T}\\ \Delta\mathbf{q}\end{bmatrix}=\begin{bmatrix}\mathbf{F}_1\\ \mathbf{F}_2\end{bmatrix}, \tag{11}$$

where

$$\mathbf{F}_1=\mathbf{K}\mathbf{T}+\mathbf{A}(\mathbf{u})\mathbf{T}+\mathbf{B}\mathbf{q}=\mathbf{0}, \tag{12}$$

$$\mathbf{F}_2=\mathbf{C}\mathbf{q}+\mathbf{D}\mathbf{T}=\mathbf{0}, \tag{13}$$

$$\mathbf{J}=\begin{bmatrix}\dfrac{\partial\mathbf{F}_1}{\partial\mathbf{T}} & \dfrac{\partial\mathbf{F}_1}{\partial\mathbf{q}}\\ \dfrac{\partial\mathbf{F}_2}{\partial\mathbf{T}} & \dfrac{\partial\mathbf{F}_2}{\partial\mathbf{q}}\end{bmatrix}. \tag{14}$$

The various entries in the Jacobian number are computed by

$$\frac{\partial\mathbf{F}_1}{\partial\mathbf{T}}=\mathbf{K}+A(u),\qquad \frac{\partial\mathbf{F}_1}{\partial\mathbf{q}}=\mathbf{B},\qquad \frac{\partial\mathbf{F}_2}{\partial\mathbf{q}}=\frac{1}{e}\mathbf{I}-\frac{1-e}{e}\mathbf{F},\qquad \frac{\partial\mathbf{F}_2}{\partial\mathbf{T}}=-4\mathbf{D}.$$

Thus equation (14) can be rewritten as

$$\begin{bmatrix}\dfrac{\partial\mathbf{F}_1}{\partial\mathbf{T}} & \mathbf{B}\\ -4\mathbf{D} & \dfrac{1}{e}\mathbf{I}-\dfrac{1-e}{e}\mathbf{F}\end{bmatrix}\begin{bmatrix}\Delta\mathbf{T}\\ \Delta\mathbf{q}\end{bmatrix}=\begin{bmatrix}\mathbf{F}_1\\ \mathbf{F}_2\end{bmatrix}. \tag{15}$$

The solution of equation (15) can be segregated in a similar manner to successive substitution as follows:

$$\frac{\partial \mathbf{F}_1}{\partial \mathbf{T}}\Delta\mathbf{T} = \mathbf{F}_1 - \mathbf{B}\Delta\mathbf{q}, \tag{16}$$

$$\left(\frac{1}{e}\mathbf{I} - \frac{1-e}{e}\mathbf{F}\right)\Delta\mathbf{q} = \mathbf{F}_2 - 4\sigma(\mathbf{I}-\mathbf{F})\mathbf{T}^3\Delta\mathbf{T}, \tag{17}$$

$$\mathbf{T}^{i+1} = \mathbf{T}^i + \Delta\mathbf{T},$$

$$\mathbf{q}^{i+1} = \mathbf{q}^i + \Delta\mathbf{q}.$$

Again equation (17) is solved first and then the results are used to solve equation (16).

Numerical damping

Owing to the high non-linearity of the radiation exchange equations, in particular the dependence on T^4, we have found that the use of relaxation (i.e. numerical damping) during the solution iteration process is almost mandatory. The relaxation is performed in a standard fashion as follows:

$$\mathbf{q}_{i+1} = (1-a)\mathbf{q}^*_{i+1} + a\mathbf{q}_i,$$

i.e. after solving for the solution $\mathbf{q}^*_{i+1}$ at iteration $i+1$, the final solution $\mathbf{q}_{i+1}$ at this iteration is formed from $\mathbf{q}^*_{i+1}$ and the solution at the previous iteration $\mathbf{q}_i$ using the foregoing equation. a is the relaxation factor, where zero corresponds to no relaxation, i.e. $\mathbf{q}_{i+1} = \mathbf{q}^*_{i+1}$, and unity to the other extreme, i.e. $\mathbf{q}_{i+1} = \mathbf{q}_i$. In most of the simulations presented in this paper a relaxation factor between 0·3 and 0·9 was employed.

Macrosurface

As described above, the side (or face) of each element on the boundary of the fluid domain may be considered as a radiating surface. In order to reduce the view factor computation cost, if temperature does not vary significantly over a part of the boundary, an alternative approach is to 'lump' together elements on the boundary and consider this group of element sides as a 'macrosurface' for radiation exchange and view factor computation purposes. This approach substantially reduces the size of the matrices $\mathbf{A}_{22}$ and $\mathbf{D}$. Another advantage is that the number of view factors that must be calculated can be significantly reduced.

Thus a macrosurface is a collection of adjacent element sides (in 2D) or element faces (in 3D). Each element side (or face) has various quantities such as area, temperature, emissivity, etc. associated with it. In order to use the macrosurface approach, each macrosurface must have an effective temperature and emissivity associated with it. Given a quantity ϕ_k associated with node k of an element side (or face) i, the effective value of this quantity, Φ, for the macrosurface comprised of N element sides is computed by

$$\Phi = \frac{1}{A_S}\sum_{i=1}^{N} A_i\left(\sum_{k=1}^{n} c_{ik}\phi_k\right), \tag{18}$$

where A_i is the area of element i, A_S is the area of the macrosurface (i.e. $\sum A_i$), N is the number of elements in the macrosurface, n is the number of nodes in each element, $c_{ik} = (\int \vartheta_{ik}\,\mathrm{d}A)/A_i$ is an 'averaged' shape function for element i and ϑ_{ik} is the shape function at node k of element i.

Thus equation (18) can be used to 'lump' the elemental quantities of temperature or emissivities into surface quantities. These values are then used in equation (10) or (17) to calculate the heat flux. This heat flux is assumed to be constant for all the elements comprising the surface. The elemental values for heat flux due to radiation can then be used as boundary conditions for the energy equation.

Radiation boundary conditions at inflows and outflows

When simulating fluid flows, the computational domain is often truncated relative to the physical domain; also, the computational domain often includes boundaries where inflow or outflow of fluid is taking place. Since the radiation exchange equation (2) is based on a closed enclosure assumption, some modification must be made to accommodate such openings or 'windows'. The boundary condition for heat exchange at such an opening must not allow any emission of energy back into the enclosure.

The derivation of the correct boundary condition is straightforward: consider the configuration shown in Figure 4.

Let the opening surface be i and assume that there is a plane parallel to surface i at infinity such that the view factors between the surface i and the rest of the enclosure are identical to the view factors between the surface at infinity and the rest of the enclosure. The heat exchange Δq_k between a typical surface k and the surface at infinity (assuming that the surface at infinity is black) is given by

$$\Delta q_k = \sigma F_{ik}(T_\infty^4 - e_k T_k^4), \tag{19}$$

where T_k is the temperature of surface k and T_∞ is the radiation source/sink reference temperature for the opening.

The total heat exchange between the surface i and the surface at infinity is the sum of the Δq_k for all surfaces k, i.e.

$$q_i = \sum_{k=1}^{N} \Delta q_k. \tag{20}$$

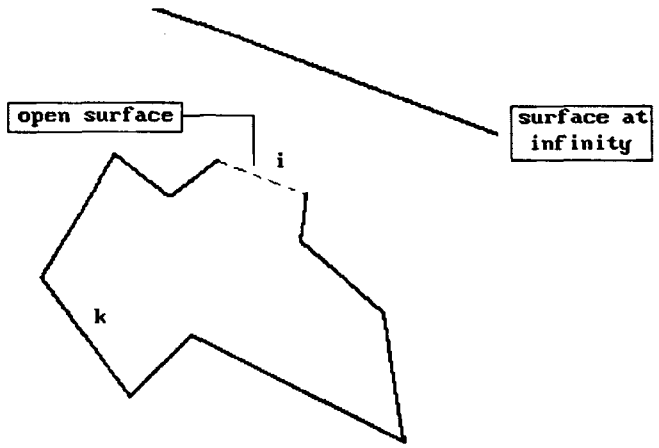

Figure 4. Opening boundary condition

Substituting equation (19) in equation (20), we arrive at the result for the total heat flux through the opening surface i:

$$q_i = \sigma T_\infty^4 - \sum_{\substack{j=1 \\ i \neq j}}^{N} \sigma e_j F_{ij} T_j^4.$$

This value of q_i is applied as a boundary condition for the solution of equation (2). One should note that since the medium is non-participating, the fluid temperature at the opening is not directly affected. Morevoer, any applied fluid temperature does not directly interface with radiation at that boundary.

EXAMPLES AND ILLUSTRATIONS

To validate and illustrate the implementation described in the previous sections, the solutions to five example problems are presented in this section. The first problem is a simple problem with an analytical solution that serves as a test case for verifying the opening/window boundary condition. The second and third examples are problems that have been studied by Holland *et al.*[8] and Kassemi and Duval[9] and serve as benchmark problems for testing the accuracy of the algorithm. The fourth problem is flow over a heat-generating step in a vertical channel. The last problem is a more realistic problem from the field of electronics packaging consisting of the flow of air past multiple heat-generating chips surrounded by walls of porous material. This problem involves conduction within the solid, porous and fluid materials as well as convection within the fluid. As well as radiation boundary conditions, convection-cooling boundary conditions, are also present on the outside walls.

The first four problems were run in a non-dimensional form appropriate to the problem under consideration. Depending on the problem, the non-dimensional numbers involved include the Peclet, Prandtl, Rayleigh and/or Reynolds numbers. When equation (2) is cast in non-dimensional form, a non-dimensional coefficient *Rad* appears as the coefficient of the T^4-term. *Rad* is defined by

$$Rad = \frac{\sigma T_{\text{ref}}^3 L}{k}.$$

Rad can be thought of as a non-dimensional 'Stefan–Boltzmann' constant and we will refer to it as the Radiation number.

In all the simulations described in this paper, four-node linear quadrilateral finite elements have been employed, although the algorithm has been implemented for linear and quadratic quadrilaterals and triangles.

Pan-in-the-desert problem

It is well known that in a desert, water in a pan can freeze at nights in ambient temperatures which are well above the freezing point of water owing to the radiation of heat to the environment. This phenomenon is simulated here for a quasi-one-dimensional case where the surface of the pan radiates heat energy to the environment. The geometry and boundary conditions are summarized in Figure 5(a). For simplicity, two major assumptions were made: no convection in the fluid and no convective heat transfer from the top surface of the fluid to the environment. In other words, only the energy equation with the appropriate boundary conditions needs to be solved. The boundary conditions include an applied temperature at the top surface and a flux boundary condition at the bottom surface. This flux is the same as the heat radiating

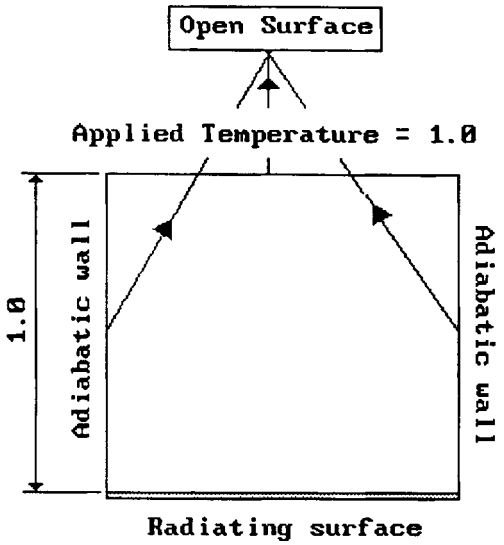

Figure 5(a). Pan-in-the-desert model

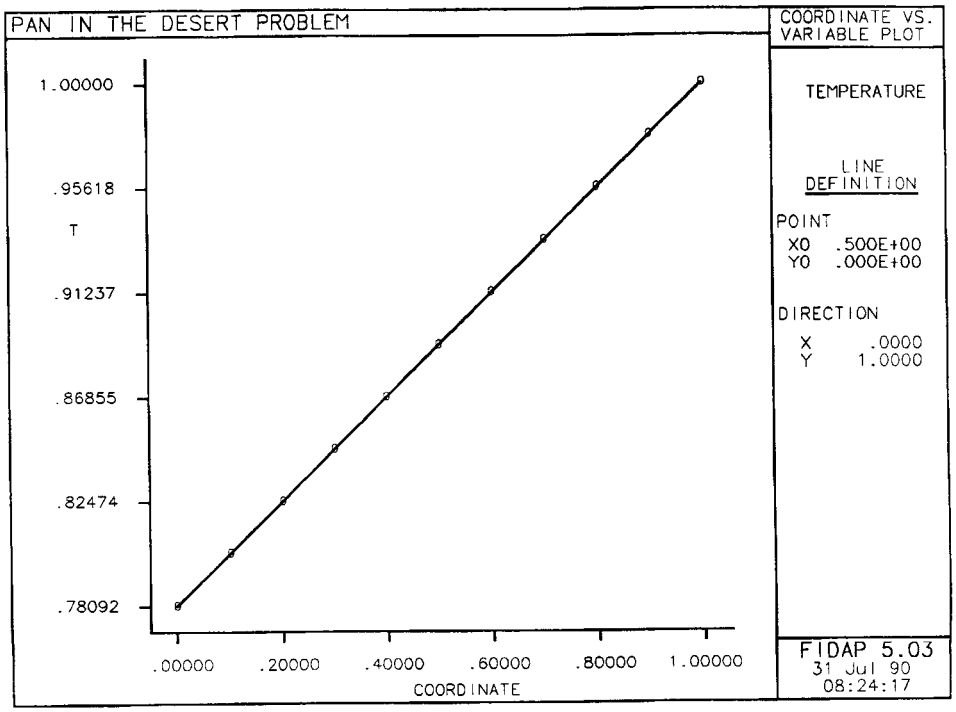

Figure 5(b). Pan-in-the-desert problem: temperature profile

from the bottom of the pan ($q = \sigma(T^4 - T_0^4)$, where T_0 is the temperature at infinity). The problem was solved in a non-dimensional form with the computational domain being a square of height of 1·0. The finite element model had 10 elements horizontally and 10 elements vertically. The boundary conditions were adiabatic on the vertical sides and an applied temperature of 1·0 at the top surface. The grey-body radiation surfaces were the bottom surface, which was assumed to be black, and the other three boundaries, which were declared as open surfaces with a sink temperature of zero. The Radiation number was 0·588 766. The computed solution using the proposed method resulted in a temperature of 0·7809 for the bottom surface, which is about 22% lower than the ambient value. The analytical solution, which is obtained by solving the one-dimensional heat conduction equation subjected to the flux boundary described above, produces a value of 0·7809 for the temperature of the pan surface. A plot of the temperature distribution vertically through the fluid is shown in Figure 5(b).

Solar panel collector

This example was suggested by Holland *et al.*[8] and models the heat transfer problem in a single solar panel collector cell. The geometry and boundary conditions are summarized in Figure 6(a). In this problem convection plays a relatively minor role and is ignored. Therefore the momentum and continuity equations are not solved and the convective term is dropped from the energy equation. Holland *et al.* studied the variation of the radiation heat transfer coefficient between the end surfaces as a function of several variables such as surface finish, specular dependence, etc. Herein, one of Holland's test cases was duplicated in order to verify the implementation of the algorithm. It should be mentioned that his numerical formulation is based on a specular wall surface; however, the end plates can be modelled as either diffuse or specular. Therefore a certain amount of discrepancy between the results of his model and this formulation is to be expected. The panel cell was a cylinder with a radius of 0·0053 m and a length of 0·0633 m—for modelling purposes an axisymmetric geometry was assumed. The finite element mesh employed had 10 elements in the radial direction and 50 elements in the axial direction. The problem was modelled with a wall surface emissivity of 0·45 and three different end surface emissivities of 0·88/0·88, 0·88/0·065 and 0·065/0·065, respectively, where the first number refers to the emissivity of the cold plate and the second one refers to the emissivity of the hot plate. (Again, in Holland's formulation the value of 0·065 indicates the specular dependence of the surface.) The end surfaces had an applied temperature of 306 on one end and an applied temperature of 298 on the other end. For grey-body radiation purposes each end plane was specified as one macrosurface and the shell of the cylinder was divided into 10 radiation surfaces. The problem was non-dimensionalized using

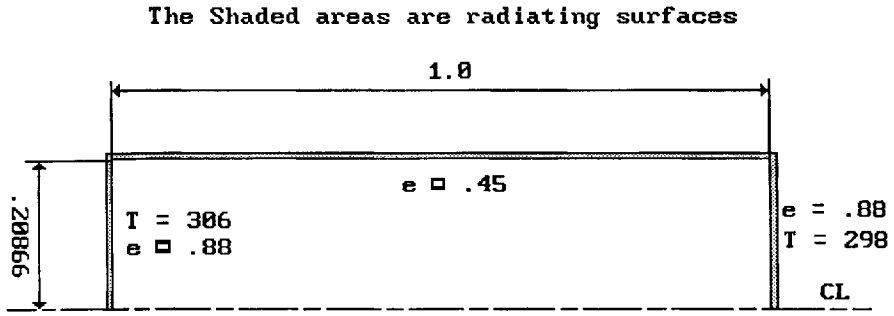

Figure 6(a). Solar panel collector model

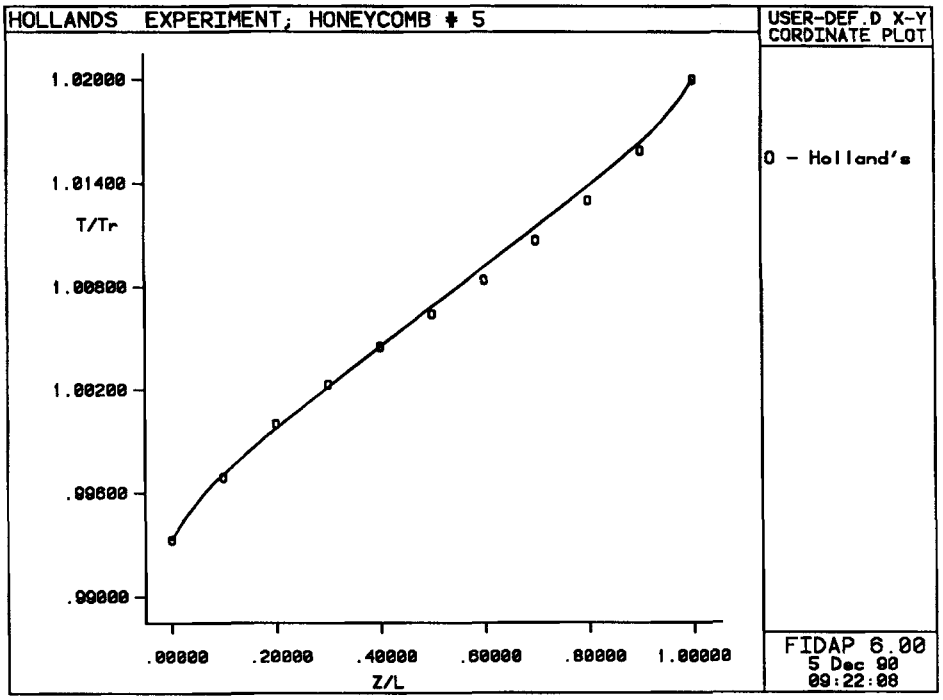

Figure 6(b). Solar panel collector: axial temperature variation, hot wall emissivity 0·88, cold wall emissivity 0·88

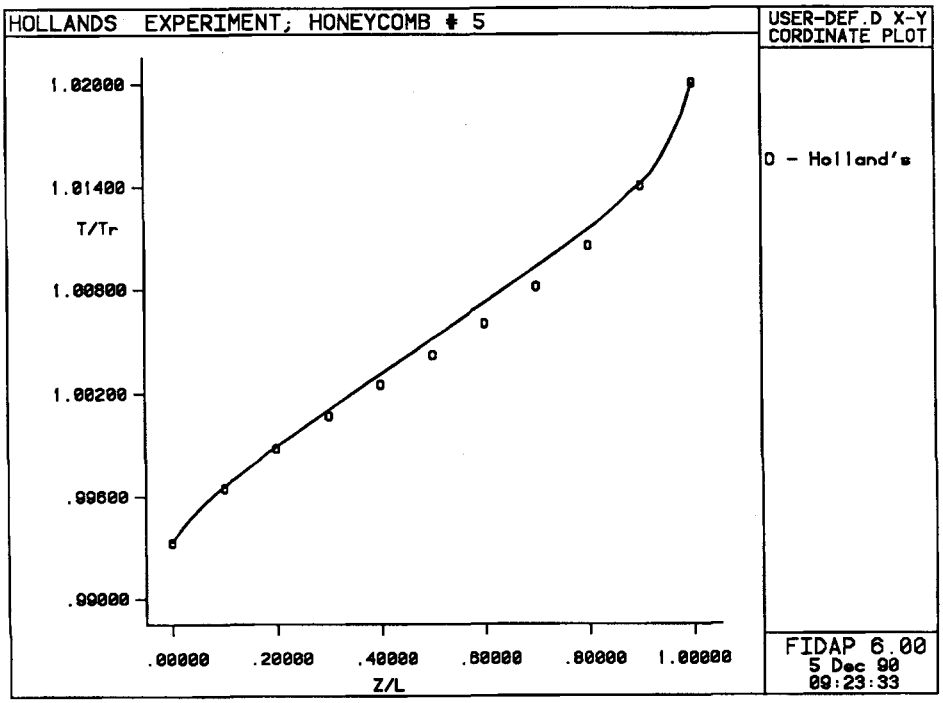

Figure 6(c). Solar panel collector: axial temperature variation, hot wall emissivity 0·88, cold wall emissivity 0·065

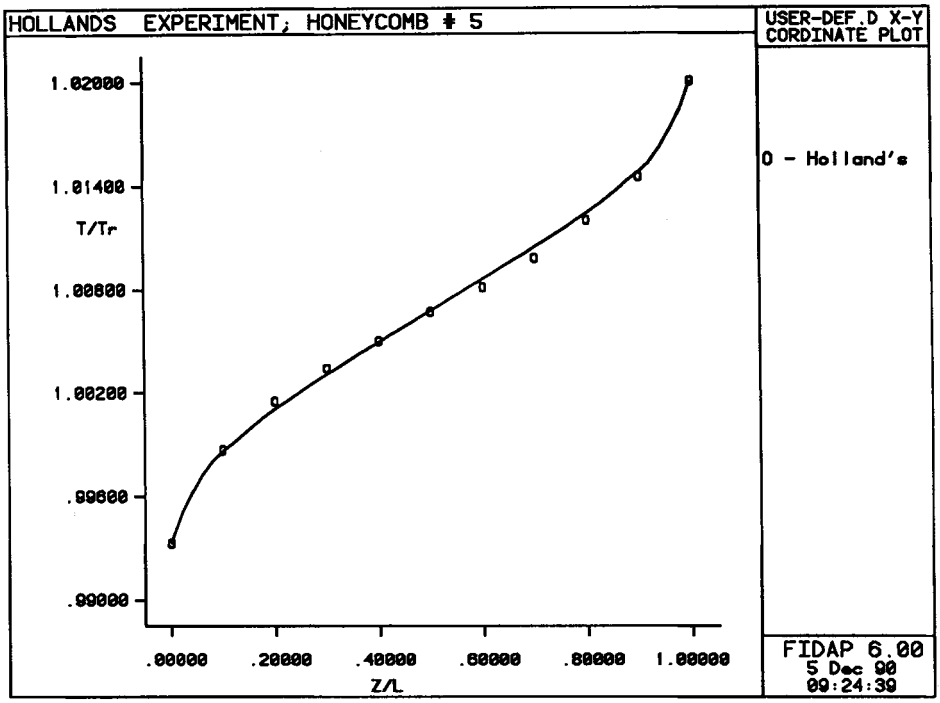

Figure 6(d). Solar panel collector: axial temperature variation, hot wall emissivity 0·065, cold wall emissivity 0·065

a characteristic length of 0·01 m and a characteristic temperature of 300 degrees. The resultant Radiation number was 0·588 766. The computed temperature distribution matched Holland's reported results within 2%. The solution procedure employed was successive substitutions (each case converged to a residual of $1{\cdot}0 \times 10^{-4}$ in the solution vector in eight iterations) with a relaxation factor of 0·3. A plot of the temperature as a function of the distance between the end plates is presented in Figures 6(b)–6(d).

Crystal growth problem

Kassemi and Duval[9] studied the effects of radiation in a crystal growth environment. In this problem the effect of convection which was ignored in the previous cases is now taken into consideration. Therefore both the continuity and momentum equations are solved. The velocity boundary conditions employed here do not exactly match those of Kassemi; in his work he assumed that material dissolves from the hot vertical wall and deposits on the cold opposing wall. Since this species removal and deposit is relatively slow, for the sake of modelling simplicity we have ignored this effect. Therefore the velocity boundary conditions employed are no-slip conditions on all walls. The crystal geometry was 5·0 by 1·0 and the finite element mesh employed had 32 elements in the x-direction and 16 elements in the y-direction. The temperature boundary conditions were 1·0 on the hot vertical wall and 0·7 on the cold wall. Grey-body radiation boundary conditions were specified for all walls. Reference 9 presents the results for a number of test cases. The case simulated here is for a Grashof number $Gr = 1{\cdot}0 \times 10^5$ and $Nr = 10$. Nr is a non-dimensional radiation–conduction parameter which shows the relative importance of radiation to conduction. This number is similar to the Radiation number mentioned earlier. These

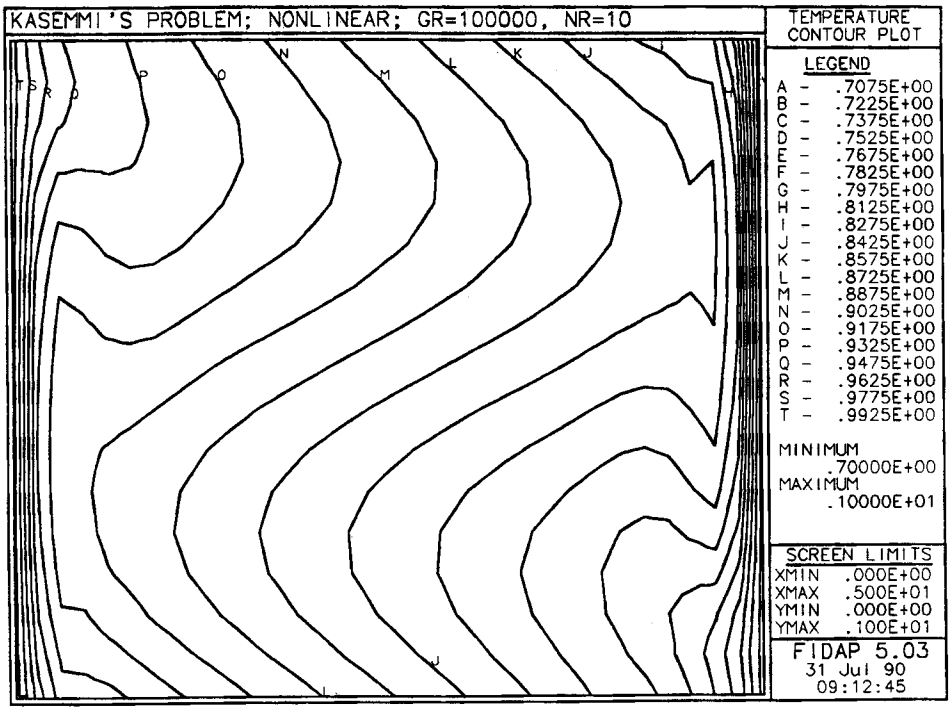

Figure 7(a). Kassemi's crystallization problem: temperature contour plot

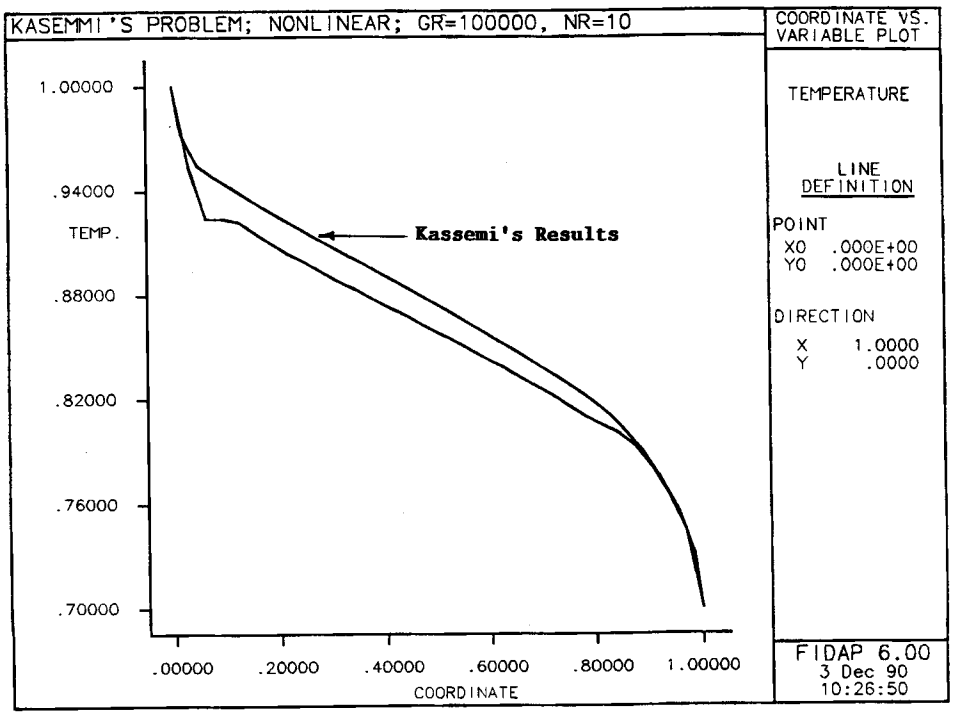

Figure 7(b). Kassemi's crystallization problem: temperature along the bottom wall

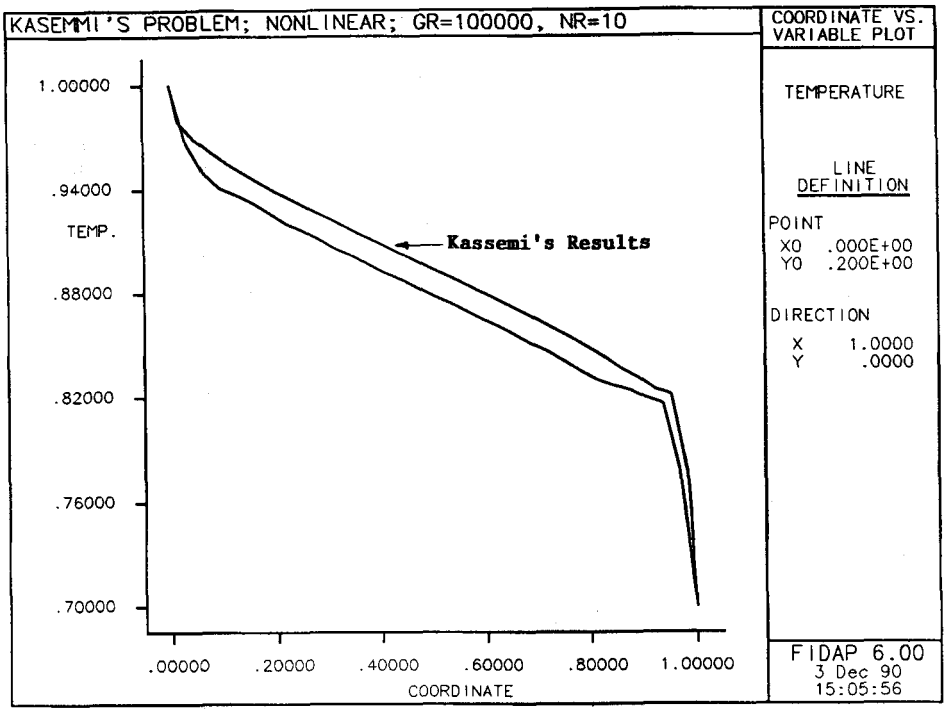

Figure 7(c). Kassemi's crystallization problem: temperature along the top wall

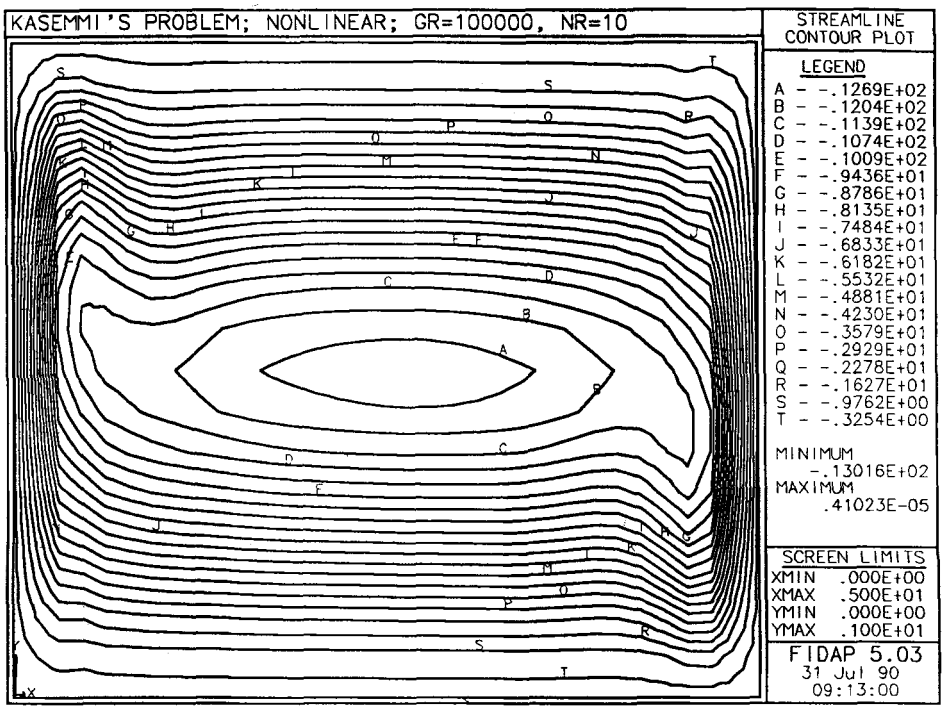

Figure 8. Kassemi's crystallization problem: streamline contour plot

values are equivalent to a Radiation number of 3·0 (reference temperature of 1000), a Reynolds number of 1·4286, a Prandtl number of 0·7 and a Rayleigh number of $2{\cdot}33 \times 10^5$. Each vertical wall is considered to be a single radiation macrosurface and each horizontal wall 10 surfaces. All radiation surfaces are assumed black. In this problem the Navier–Stokes equations including buoyancy effects together with the energy equation were solved. Eighteen iterations were required to achieve convergence using successive substitutions with a relaxation factor of 0·4. The convergence criterion was that the change in the solution vector was less than $1{\cdot}0 \times 10^{-4}$ for all solution quantities. Figures 7(a)–7(c) correspond to temperature distribution in the domain of the problem and along the bottom and top walls. Figure 8 shows the streamlines of the computed solution; these show excellent qualitative agreement with the results presented in References 9 and 17. In these plots the vertical direction has been expanded by a factor of five.

Flow in a vertical open-ended channel

In this problem the effect of different combinations of modes of heat transfer is studied. The geometry is a vertical 2D channel with a heat-generating step and convection cooling on the outer wall opposing the chip. The conditions are such that flow with a uniform temperature enters the channel, passes over the step and then leaves the system. Figure 9 shows the geometry as well as the boundary conditions and the input data. Figure 10 depicts the finite element mesh and

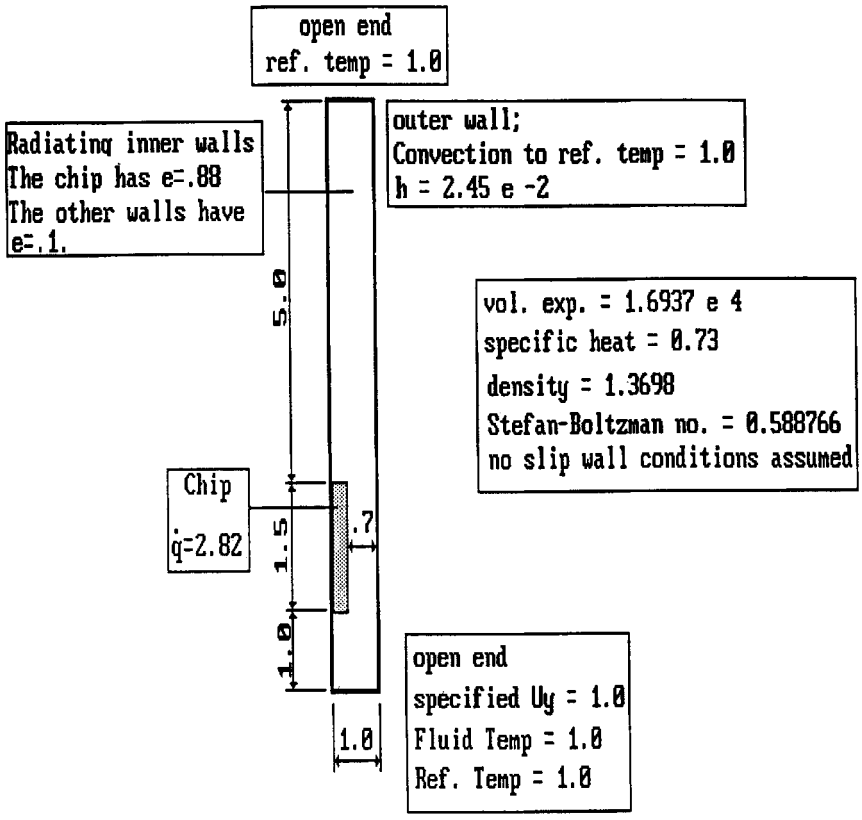

Figure 9. Open-ended channel: geometry and boundary conditions

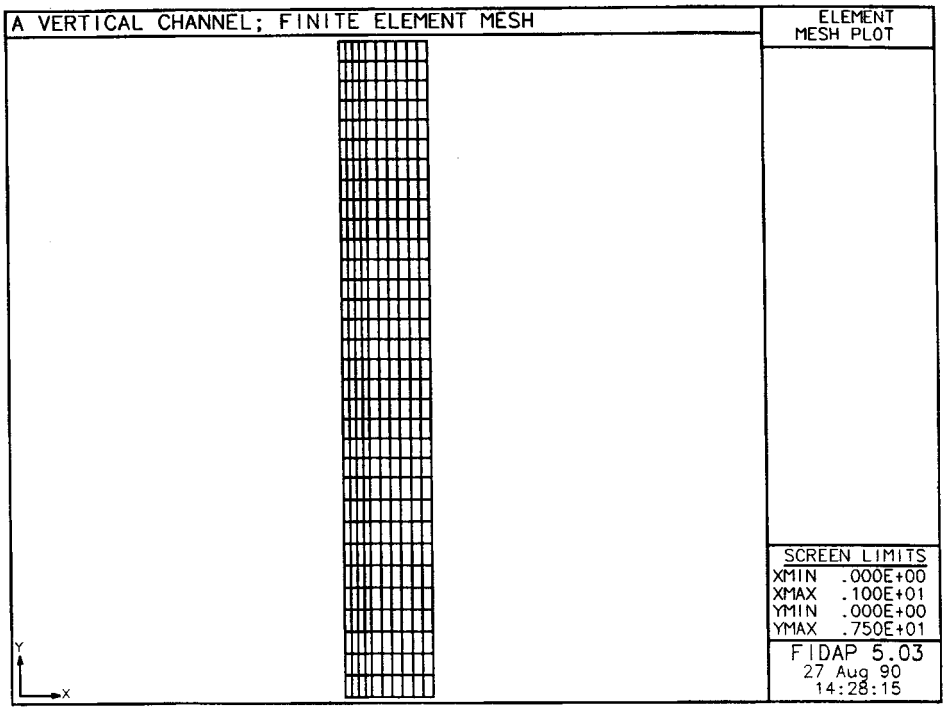

Figure 10. Open-ended channel: finite element mesh

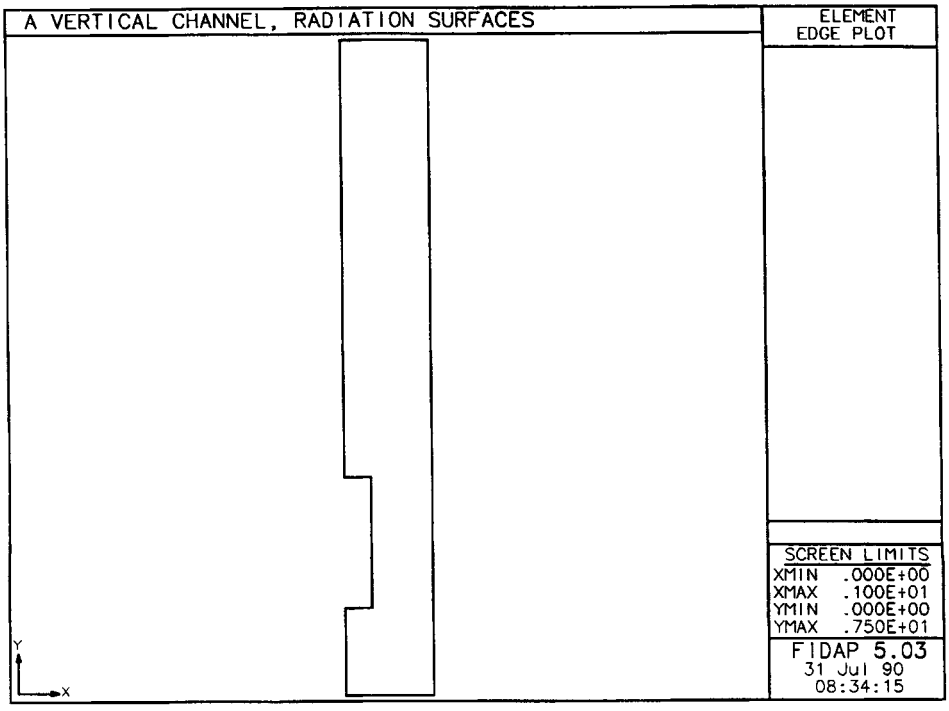

Figure 11. Radiation surfaces for the open-ended channel

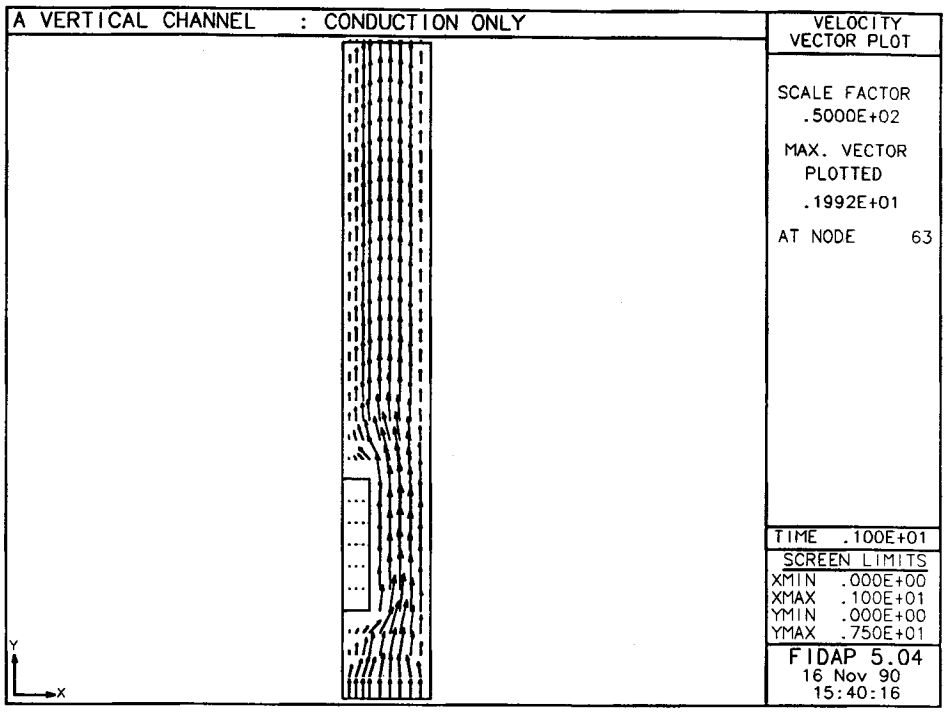

Figure 12(a). Open-ended channel: velocity profile when all modes of heat transfer are active

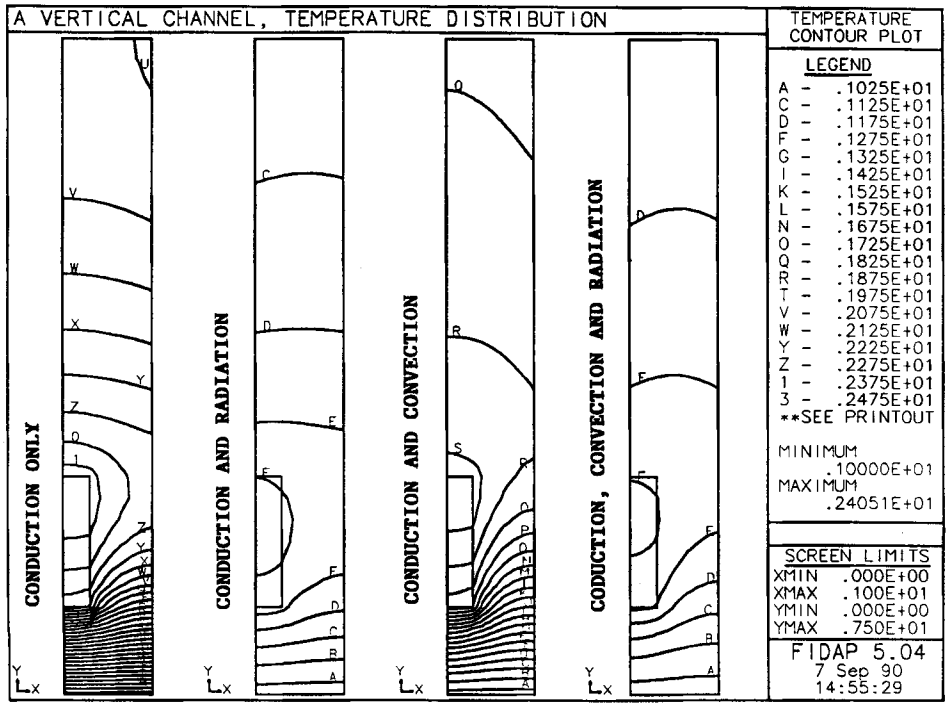

Figure 12(b). Open-ended channel: temperature distribution for the different modes of heat transfer

Figure 11 illustrates the eight radiating surfaces: each open end was specified as one macrosurface; the three surfaces that covered the step (specified as blocking) were each one macrosurface; the remaining three walls were also specified as radiating surfaces with an emissivity of 0·88. The solid was assumed to be 10 times as conductive as the fluid. A Prandtl number of 0·73 and a Reynolds number of 1·3698 were specified for the fluid. Four cases were studied: (a) conduction only, (b) conduction and radiation, (c) conduction and convection and (d) all three modes combined. In this analysis buoyancy effects were ignored. Successive substitution was the solution method—used with relaxation factor of 0·6 when radiation was present and 0·0 when radiation was not considered. Case (a) converged in one iteration, (b) in 10, (c) in two and (d) in nine. The convergence criterion was set to a default value of 0·001. Figure 12(a) shows the velocity field and Figure 12(b) the temperature distribution for each case. It is clear that radiation and convection both reduce the overall temperature. In this problem radiation has a dominant effect.

Electronics-packaging problem

To demonstrate the ability to analyse complex problems, a more realistic example from the field of electronics packaging was considered. A two-cell vertical channel with heat-generating

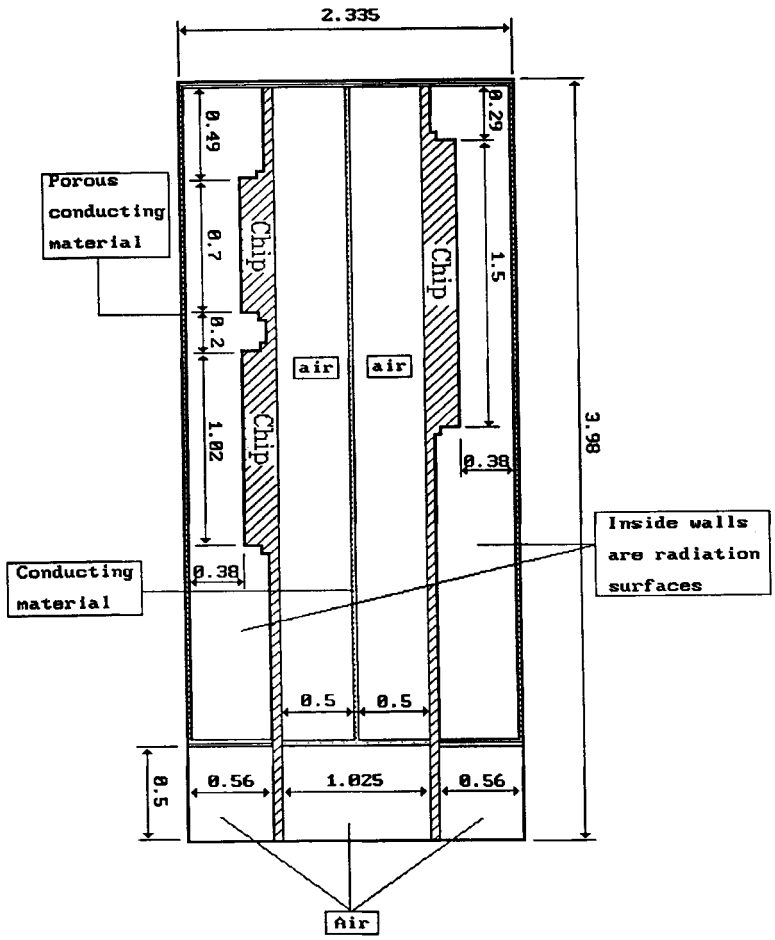

Figure 13. Electronics-packaging problem: complex geometry and boundary conditions

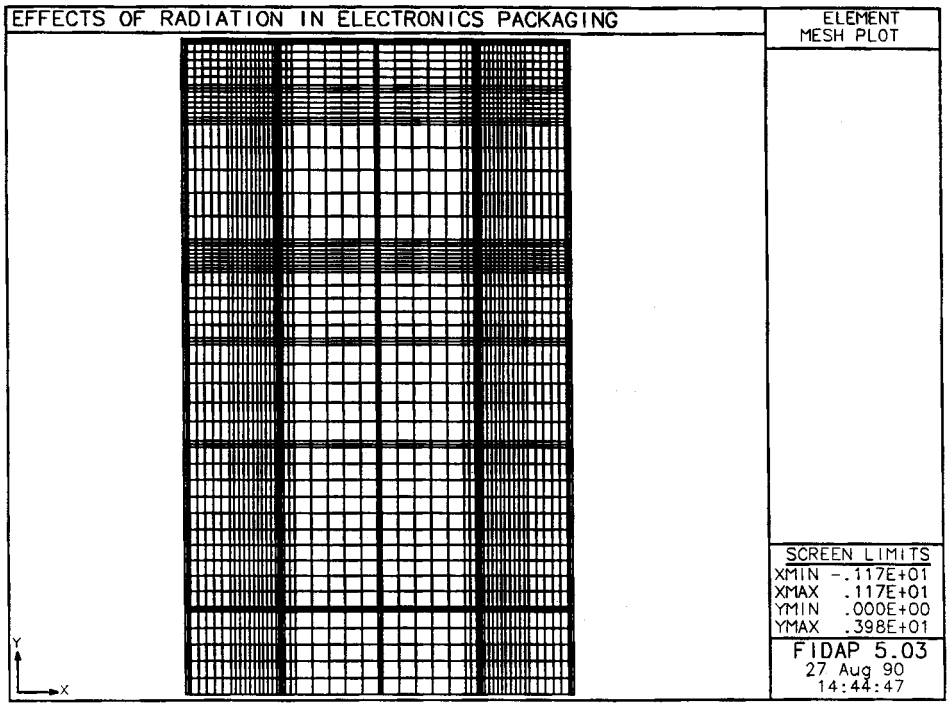

Figure 14. Electronics-packaging problem: finite element mesh

Table I. Material properties of the complex problem (all units are in watts, seconds, inches)

Properties of air

Density = $1{\cdot}929 \times 10^{-5}$
Viscosity = $4{\cdot}689 \times 10^{-5}$
Specific heat = 1005
Conductivity = $6{\cdot}655 \times 10^{-4}$
Volume expansion = 0·0033 at a reference temperature = 300

Conductivity of the solid and porous materials

Porous base = 0·94
Chip packages = 0·038
Package leads = 3·8
Central heat sink = 1·143
Caging = 1·70

Properties of the radiative surfaces

Emissivity = 0·88
Stefan–Boltzmann constant = $3{\cdot}6577 \times 10^{-11}$

Permeability of the different porous materials

Porosity = 0·48
Permeability = 10^{-5} in the direction normal to the plane of the material

Heat transfer coefficient at the outer walls

$h = 6{\cdot}45 \times 10^{-3}$ at reference temperature = 300

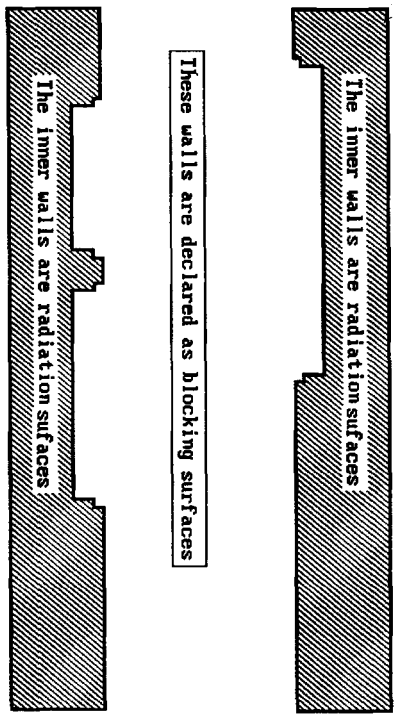

Figure 15. Electronics-packaging problem: radiation surfaces

chips was modelled; the bottom and top portions as well as the sides of the channel were comprised of porous materials. The left-hand channel had two heat-generating steps and the right-hand channel included only one chip. The two channels were connected by a heat-conducting material. The inner walls were assumed to be grey-diffuse surfaces and there was convection to the environment from the outer walls. The complete geometry is shown in Figure 13 while Figure 14 depicts the finite element mesh employed. Table I summarizes the various material properties. For this simulation the full Navier–Stokes equations including buoyancy effects and the energy equation were solved.

For radiation boundary condition specification purposes, 49 radiating surfaces were defined; these surfaces are shown in Figure 15. Note that the 27 surfaces in the middle of the computational domain were defined as blocking surfaces for view factor calculation purposes. Figure 16 shows the resultant temperature distribution for an emissivity of 0·8 while Figure 17 shows the velocity field for the fluid as it passes through the system. To investigate the effects of radiation on the resultant temperature field, three different values of wall emissivity were employed ($e=0{\cdot}1$, 0·1, 0·8). The chip emissivity remained constant ($e=0{\cdot}88$) for all three cases. Similar to the previous cases, the method of solution was successive substitution with a relaxation factor of 0·9. The no-radiation case converged in 19 iterations while the radiation cases took 44 iterations. Figure 18 shows the temperature profile over the chips and the opposing wall in the left channel while Figure 19 depicts the temperature profile over the chip and the opposing wall in the other channel. Although the results indicate that for this particular system radiation does not have a significant effect on the resultant temperature distribution, the radiative interaction between the chip and the walls becomes more influential in reducing the temperature as the wall emissivity increases.

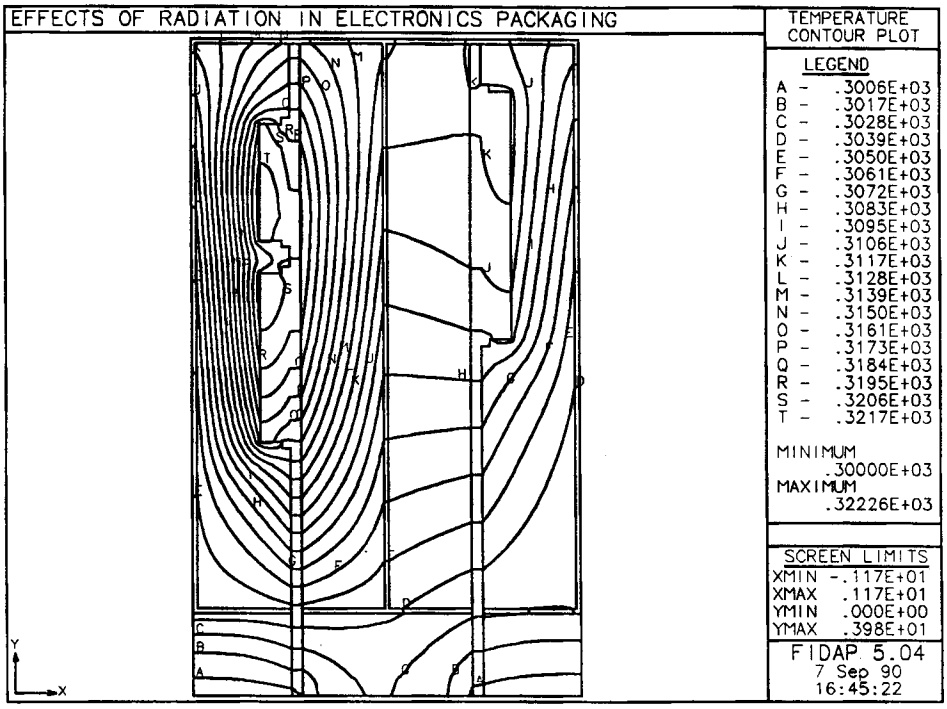

Figure 16. Electronics-packaging problem: temperature distribution

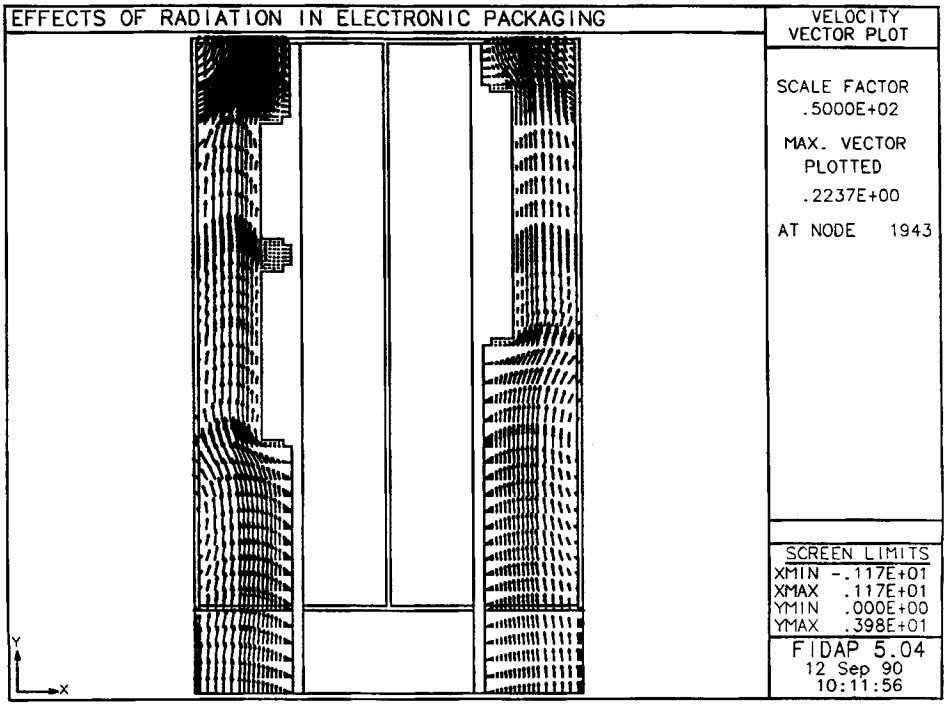

Figure 17. Electronics-packaging problem: velocity field

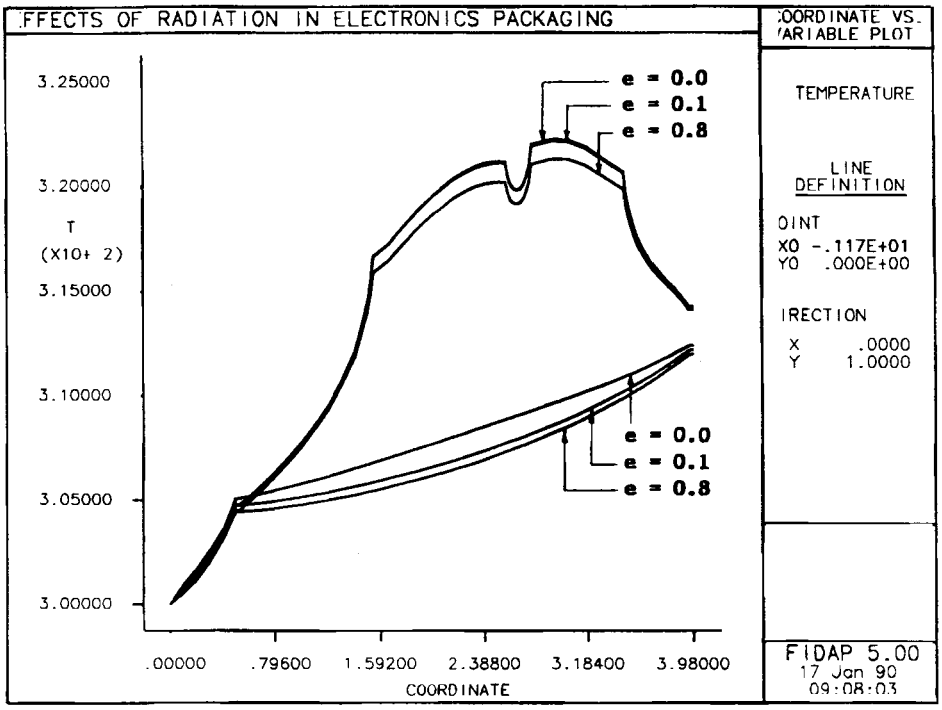

Figure 18. Electronics-packaging problem: temperature along the two chips

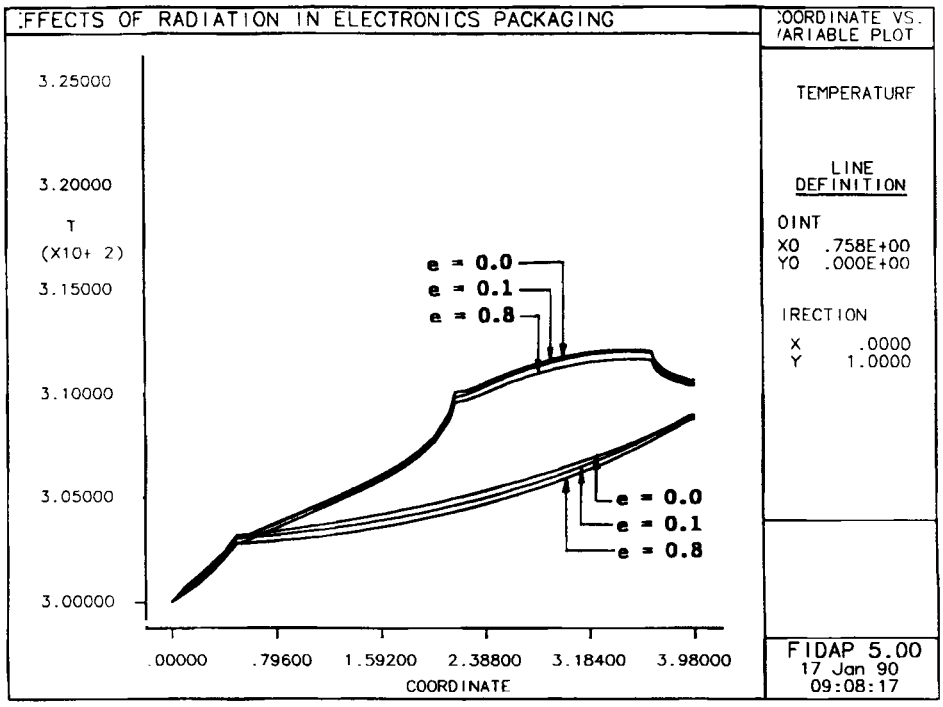

Figure 19. Electronics-packaging problem: temperature along a line over one chip

FINAL REMARKS

In this paper we have described an algorithm for solving fluid flows coupled with the grey-body radiation boundary condition. The introduction of two features—the decoupling of the solution of the radiation exchange equation from the solution of the continuum equations and the introduction of the concept of macrosurfaces—has resulted in a viable approach for solving realistic problems involving grey-body radiation exchange. We believe further algorithmic development is needed to reduce the requirement for relatively high relaxation factors to obtain convergence, which in turn results in larger number of iterations.

ACKNOWLEDGEMENT

Partial funding for this work was provided by Daimler-Benz, AG.

REFERENCES

1. Z. Tan, 'Radiative heat transfer in multidimensional emitting, absorbing and anisotropic scattering media, mathematical formulation and numerical method', *J. Heat Transfer*, **111**, 141 (1989).
2. M. N. Ozisik and V. Yener, 'The Galerkin method for solving radiation transfer in plane-parallel participating media', *J. Heat Transfer*, **104**, 351 (1982).
3. R. Fernandes and J. Francis, 'Combined conductive and radiative heat transfer in an absorbing, emitting and scattering cylindrical medium', *Trans. ASME*, **104**, 594 (1982).
4. T. J. Chung and J. Y. Kim, 'Two-dimensional, combined-mode heat transfer by conduction, convection, and radiation in emitting, absorbing and scattering media—solution by finite elements', *Trans. ASME*, **106**, 448 (1984).
5. M. E. Larsen and J. R. Howell, 'The exchange factor method: an alternative basis for zonal analysis of radiation enclosures', *Trans. ASME*, **107**, 936 (1985).
6. J. R. Howell, 'Thermal radiation in participating media: the past, the present and some possible futures', *Trans. ASME*, **110**, 1220 (1988).
7. R. Siegel and J. R. Howell, *Thermal Radiation Heat Transfer*, 2nd edn, McGraw-Hill, New York, 1981.
8. K. G. T. Holland, G. D. Raithby, F. B. Russell and R. G. Wilkinson, 'Coupled radiative and enductive heat transfer across honeycomb panels and through single cells', *Int. J. Heat Mass Transfer*, **27**, 2119 (1984).
9. M. Kassemi and W. M. B. Duval, 'Interaction of surface radiation with convection in crystal growth by vapor transport', *AIAA J. Thermophys. Heat Transfer*, 4(4), 454 (1990).
10. F. Dupret, P. Nicodeme, Y. Ryckmans, P. Wouters and M. J. Crochet, 'Global modelling of heat transfer in crystal growth furnaces', *Int. J. Heat Mass Transfer*, **33**, 1849 (1990).
11. D. E. Bornside, T. A. Kinney and R. A. Brown, 'Finite element/Newton method for the analysis of Czochralski crystal growth with diffuse-gray radiative heat transfer', *Int. j. numer. methods eng.*, **30**, 133 (1990).
12. L. J. Atherton, J. J. Derby and R. A. Brown, 'Radiative heat exchange in Czochralski crystal growth', *J. Cryst. Growth*, **84**, 57 (1987).
13. F. Dupret, Y. Ryckmans, P. Wouters and M. J. Crochet, 'Numerical calculation of the global heat transfer in a Czochralski furnace', *J. Cryst. Growth.*, **79**, 84 (1986).
14. M. J. Crochet, F. Dupret and Y. Ryckmans, 'Numerical simulation of crystal growth in a vertical Bridgman furnace', *J. Cryst. Growth*, **97**, 173 (1989).
15. *FIDAP Theoretical Manual*, Fluid Dynamics International, Evanston, IL, 1989.
16. A. B. Shapiro, 'FACET—a radiation view factor computer code for axisymmetric, 2-D planar, and 3-D geometries with shadowing', *Lawrence Livermore Laboratory Report* UCID-19889, 1983.
17. M. Kassemi, Private communications, 1990.
18. *FIDAP Users Manual*, Fluid Dynamics International, Evanston, IL, 1989.